




Article

Hydrothermally Grown Globosa-like TiO₂ Nanostructures for Effective Photocatalytic Dye Degradation and LPG Sensing

Mutcha Shanmukha Rao ^{1,2}, Benadict Rakesh ^{1,2,*}, Gunendra Prasad Ojha ³, Ramasamy Sakthivel ^{1,2}, Bishweshwar Pant ^{3,*} and Kamatchi Jothiramalingam Sankaran ^{1,2}

¹ CSIR-Institute of Minerals and Materials Technology, Bhubaneswar 751013, India; shanmukha.2021@immt.res.in (M.S.R.); rsakthivel@immt.res.in (R.S.); kjsankaran@immt.res.in (K.J.S.)

² Academy of Scientific and Innovative Research (AcSIR), Ghaziabad 201002, India

³ Carbon Composite Energy Nanomaterials Research Center, Woosuk University, Wanju 55338, Republic of Korea; gpojha10@gmail.com

* Correspondence: benadict@immt.res.in (B.R.); bisup@woosuk.ac.kr (B.P.); Tel.: +91-7708639831 (B.R.)

Abstract: The rapid expansion of industrial activities has resulted in severe environmental pollution manifested by organic dyes discharged from the food, textile, and leather industries, as well as hazardous gas emissions from various industrial processes. Titanium dioxide (TiO₂)-nanostructured materials have emerged as promising candidates for effective photocatalytic dye degradation and gas sensing applications owing to their unique physicochemical properties. This study investigates the development of a photocatalyst and a liquefied petroleum gas (LPG) sensor using hydrothermally synthesized globosa-like TiO₂ nanostructures (GTNs). The synthesized GTNs are then evaluated to photocatalytically degrade methylene blue dye, resulting in an outstanding photocatalytic activity of 91% degradation within 160 min under UV light irradiation. Furthermore, these nanostructures are utilized to sense liquefied petroleum gas, which attains a superior sensitivity of 7.3% with high response and recovery times and good reproducibility. This facile and cost-effective hydrothermal method of fabricating TiO₂ nanostructures opens a new avenue in photocatalytic dye degradation and gas sensing applications.

Keywords: titanium dioxide; hydrothermal method; nanostructures; photocatalytic dye degradation; gas sensor



Citation: Rao, M.S.; Rakesh, B.; Ojha, G.P.; Sakthivel, R.; Pant, B.; Sankaran, K.J. Hydrothermally Grown Globosa-like TiO₂ Nanostructures for Effective Photocatalytic Dye Degradation and LPG Sensing. *Molecules* **2024**, *29*, 4063. <https://doi.org/10.3390/molecules29174063>

Academic Editors: Jianbo Jia and Yong Shao

Received: 22 July 2024

Revised: 20 August 2024

Accepted: 20 August 2024

Published: 27 August 2024



Copyright: © 2024 by the authors. Licensee MDPI, Basel, Switzerland. This article is an open access article distributed under the terms and conditions of the Creative Commons Attribution (CC BY) license (<https://creativecommons.org/licenses/by/4.0/>).

1. Introduction

Environmental pollution, water scarcity, and wastewater management pose a critical convergence of threats to both human and ecological health. Exponential population growth and rapid industrial development have led to the release of organic pollutants such as methylene blue, methyl orange, congo red, rhodamine B, and crystal violet dyes into water bodies, thereby disrupting aquatic ecosystems [1]. Additionally, industrial activities, wildfires, and volcanic eruptions introduce a diverse range of contaminants into the environment [2]. The subsequent dissemination of noxious gases resulting from these activities significantly impacts living organisms, posing considerable health risks [3]. Metal oxides, particularly TiO₂, ZnO, WO₃, In₂O₃, SnO₂, and Fe₂O₃ have dominated photocatalysis and gas sensing applications due to their abundance, affordability, and ability to tailor their properties for specific needs [4,5]. Among the various metal oxide nanostructured materials, TiO₂ nanostructures constitute a versatile material with significant potential in environmental remediation, clean energy generation, and consumer products. The wide band gap and potent oxidation power of TiO₂, when activated by ultraviolet (UV) or visible light irradiation, demonstrates significant promise for addressing environmental challenges through its photocatalytic and gas sensing capabilities [6–8]. However, TiO₂ films face challenges such as slow response and recovery times, low sensitivity, poor selectivity, and the need for high operating temperatures. This understanding has spurred the development

of nanostructured TiO₂ with diverse morphologies (nanoflowers, nanowires, nanosheets, nanorods, etc.).

Nanostructured TiO₂ photocatalysts have garnered considerable attention due to their unique morphologies and properties [9]. These nanostructures possess a significantly increased surface area compared to their bulk counterparts, providing abundant active sites for light absorption and reactant interaction. Since its pioneering discovery by Fujishima and Honda in the early 1970s, the photocatalytic activity of TiO₂ has undergone significant advancements [10,11]. H. Almohamadi et al. [9] reported that the efficacy of the TiO₂ photocatalyst is also intrinsically linked to its structural characteristics. Hao et al. [12] reported the effect of overlayers TiO₂ and underlayer CuO on film morphology and the photocatalytic activity of the nanocomposite materials. Montero et al. [13] reported that the surface micro-nanostructuring of TiO₂ films, studying the photocatalytic properties of formic acid degradation under UV light. On the other hand, environmental concerns are driving the development of advanced gas sensing devices to detect hazardous gases like LPG, H₂S, CO, and NH₃. These devices play a vital role in safety, pollution monitoring, and industrial control. Recently, it is reported that TiO₂ nanostructures have shown significant potential in detecting a variety of gases, including NO_x, CO, H₂S, NH₃, acetone, ethanol, CH₄, and H₂ [14], because of their enhanced surface area and high sensitivity [15].

Despite extensive research on TiO₂ for photocatalysis and gas sensing applications, the primary challenge is in the fabrication of these TiO₂ nanostructures. TiO₂ nanostructures can be synthesized using methods such as hydrothermal synthesis, chemical vapor deposition, sol-gel, pulse laser deposition, electrodeposition, RF sputtering, and DC sputtering [7,16,17]. Particularly, hydrothermal synthesis offers a versatile and efficient method for creating TiO₂ nanostructures [18]. This technique allows for precise control over the material's properties, making it valuable for developing advanced materials with diverse applications [19]. A key advantage lies in its ability to tune crystallinity and morphology by adjusting reaction parameters like temperature, pressure, and duration [20]. Notably, the autoclave's pressure increases alongside temperature, exceeding the boiling point of water [19].

Herein, this work demonstrates a cost-effective fabrication of hydrothermally synthesized TiO₂ nanostructures that exhibit promising photocatalytic activity and LPG sensing capabilities. The well-defined globosa flower-like TiO₂ nanostructures (GTNs), having a high ratio of oxidative-to-reductive surface sites, promote efficient oxidation and reduction reactions during photocatalysis and gas sensing, respectively. The mechanism of the formation of globosa flower-like TiO₂ nanostructures, along with the enhanced photocatalytic dye degradation as well as superior LPG sensing characteristics are explored.

2. Results and Discussion

2.1. Materials Characteristics

The surface morphology of GTNs was examined using the plain-view FESEM. Figure 1a reveals the formation of uniformly distributed globosa flower-like nanostructures of TiO₂ on glass substrate. A well-aligned configuration of GTNs refers to an arrangement where the individual nanorods, which resemble flower petals, exhibit a preferred orientation relative to a specific axis. The magnified plain-view FESEM image shown in the inset of Figure 1a represents the nanopetals of GTNs with a diameter of ~250 nm and length of around 2.1 μm. The height of the GTNs was 8.4 μm, which was determined from the cross-sectional view FESEM micrograph shown in Figure 1b. The FESEM-EDX spectrum shown in Figure 1c confirms the presence of Ti, O, and Si elements in the GTNs. The specific surface area (SSA) of GTNs was determined (using ImageJ software-1.54j version) to be up to 0.921 m²/g [21]. The surface area analysis was conducted on GTNs by using the FESEM plot profiles. (Detailed geometrical calculations of SSA are provided in the Supporting Information). Figure 1c shows the intense Si line corresponding to the underlying glass substrate, upon which the GTNs were grown. EDX can provide valuable qualitative and semi-quantitative information about the elemental composition of GTNs. Improving the EDX quantification of GTNs depends on several factors

such as sample preparation, detector efficiency, and optimizing the beam energy [22]. At high temperatures and autogenous pressure under hydrothermal conditions, oxygen from the TiO_2 film can diffuse into the glass substrate, creating an oxygen-rich interface [23]. Figure 1c shows the obtained wt.% and at.% of EDX data corresponding to Ti, O, and Si. The TiO_2 nanorod was oriented along the [001] crystallographic direction and projected on the [110] zone axis (Figure 1d), which is in good agreement with the FESEM micrographs (Figure 1a,b). Figure 1e displays the selective area electron diffraction (SAED) pattern of GTNs, revealing the single-crystalline nature of the material. The SAED pattern confirms the growth of tetragonal rutile GTNs. In this study, the predominant crystallographic planes of the tetragonal rutile GTN structure are identified as $(\bar{1}10)$, $(\bar{1}11)$, (002), and $(2\bar{2}0)$, respectively. Moreover, Figure 1f displays the HRTEM micrograph of the GTNs. The measured d -spacing value between the lattice planes is 2.805 Å that corresponds to the (111) lattice plane of TiO_2 .

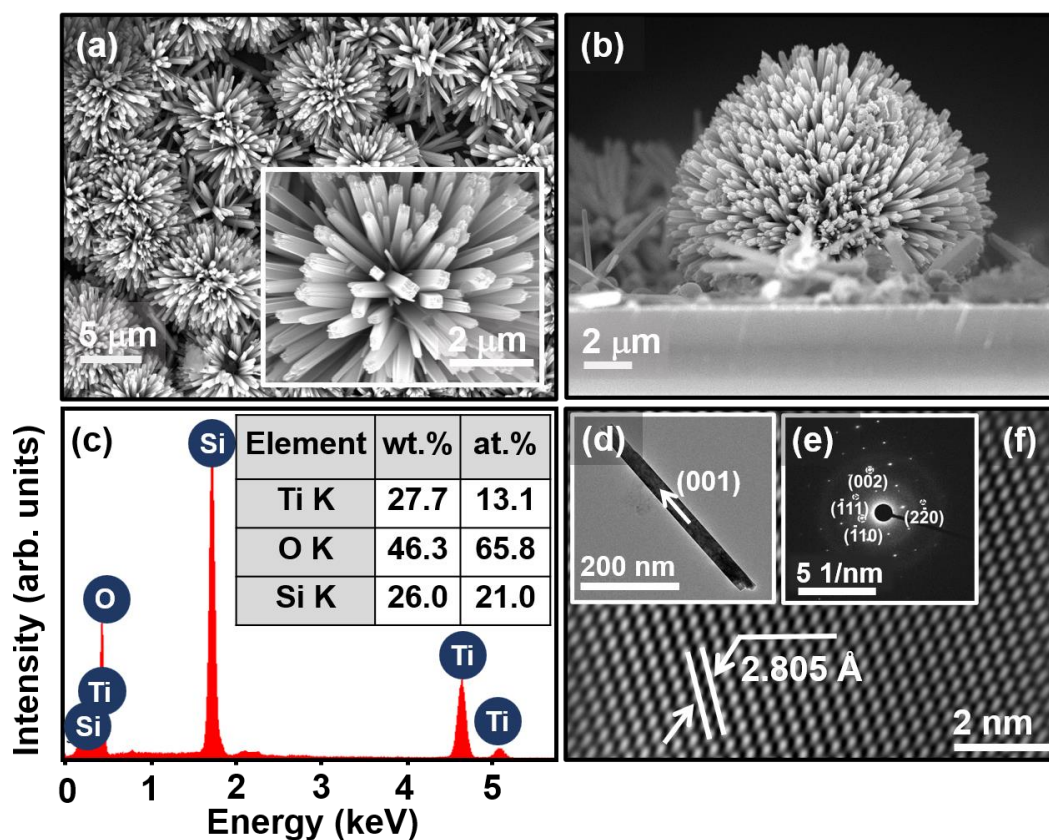


Figure 1. (a) Plain-view FESEM image of GTNs. (b) Cross-sectional FESEM image of GTNs. (c) FESM-EDX spectrum of GTNs. (d) TEM micrograph with corresponding SAED pattern of (e) GTNs synthesized using hydrothermal method. (f) HRTEM micrograph of the selected lattice fringes area of GTNs.

As shown in Figure 2a, the XRD pattern of the GTNs shows peaks at Bragg diffraction angles (2θ) of 27.4° , 36.0° , 41.3° , 54.4° , and 69.0° , corresponding to the Miller indices of the (110), (101), (111), (211), and (112) planes, respectively, which are characteristic of the rutile phase. GTNs in the tetragonal phase (JCPDS: 01-076-0321, space group: $P4_2/mnm$) had unit cell parameters $a = b = 4.625 \text{ \AA}$, $c = 2.9878 \text{ \AA}$. The investigation of GTNs using XRD analysis, along with FESEM-EDX and HRTEM, confirms the formation of rutile GTNs.

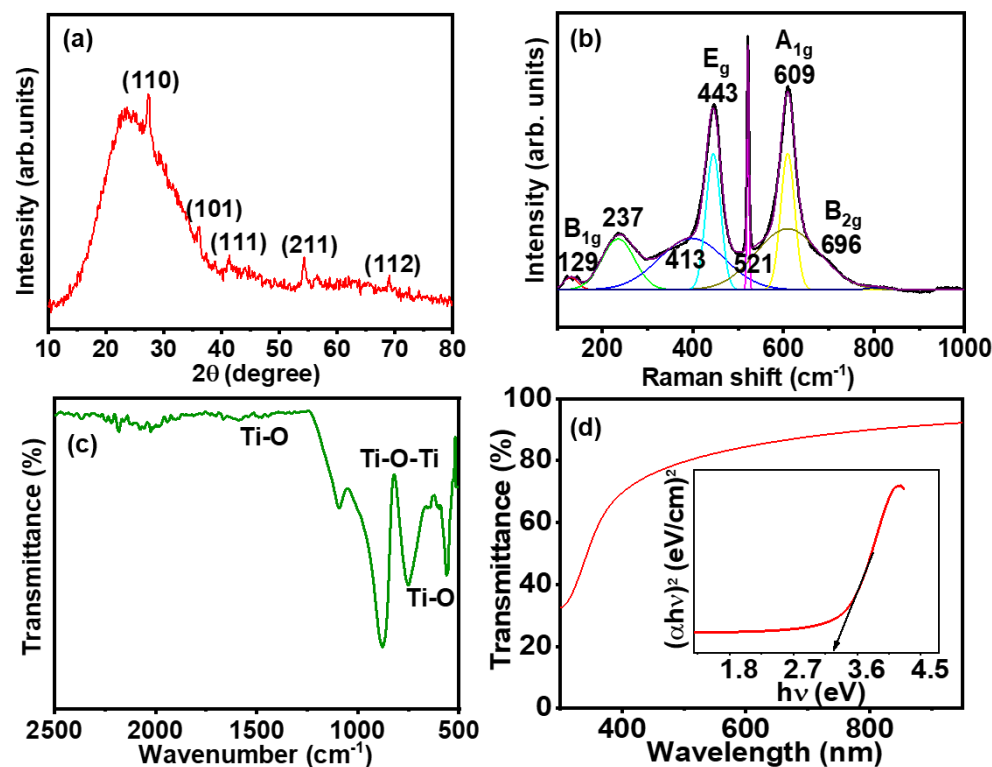


Figure 2. (a) XRD pattern, (b) Raman spectrum, (c) FTIR spectrum, and (d) UV-vis transmittance spectrum of GTNs. The inset of (d) shows the estimation of optical bandgap of GTNs.

Raman scattering was employed on the GTNs to identify the vibrational modes of the material [24]. Figure 2b exhibited the rutile phase of TiO_2 , corroborating the findings obtained from the XRD analysis. The typical Raman active modes of anatase TiO_2 are A_{1g} , $2B_{1g}$, and $3E_g$, while the Raman active modes for rutile TiO_2 films are A_{1g} , B_{1g} , B_{2g} , and E_g [25,26]. The Raman spectrum of GTNs exhibits prominent bands at higher frequencies, specifically at 129 cm^{-1} , 443 cm^{-1} , and 609 cm^{-1} , which correspond to the B_{1g} , E_g , and A_{1g} vibrational modes of rutile TiO_2 , respectively. Additionally, minor peaks are observed at 237 cm^{-1} , 413 cm^{-1} , 521 cm^{-1} , and 696 cm^{-1} , which correspond to B_{2g} vibrational modes of rutile TiO_2 . A_{1g} and B_{1g} represent in-plane modes, while the E_g mode corresponds to the out-of-plane mode. The E_g mode involves the symmetric stretching of O–Ti–O bonds and exhibits a second-order scattering feature, with the most notable peak observed at 237 cm^{-1} . The A_{1g} and E_g modes signify the vibrational characteristics of the crystal lattice, indicative of the high crystallinity nature of the GTNs [27].

Figure 2c shows that the bands in the range 4000 cm^{-1} to 400 cm^{-1} were attributed to strong absorption and vibrational bands of GTNs. The distinct broad band peaks at 565 cm^{-1} , 730 cm^{-1} , and 882 cm^{-1} were assigned to the low-frequency bending vibrations of Ti–O and Ti–O–Ti (absorption bands). The presence of a Ti–O bond at peak at 1523 cm^{-1} confirms the formation of TiO_2 [28]. The inset of Figure 2d shows the transmittance (%) of GTNs that was calculated in the wavelength range of 300–1000 nm. The optical transmission in the UV–vis–near-infrared region is 70–90%. Figure 2d shows the UV–vis–near-infrared spectrophotometer of the GTNs. The estimated optical bandgap of the GTNs evaluated from Figure 2d using a Tauc plot [29] is 3.06 eV.

It is clearly revealed from the materials characteristics that there is a formation of well-defined single-crystalline rutile phase GTNs. However, the underlying growth mechanism for GTNs remains elusive. Basically, the formation of metal oxide nanostructures follows a rapid nucleation of small particles at the initial stage, followed by their aggregation. Subsequently, these smaller particles dissolve while larger ones grow due to Ostwald ripening and lead to the formation of nanostructures [30,31]. Moreover, Yang et al. [32]

proposed that the anisotropic growth of rutile TiO_2 nanoflower arrays is governed by the atomic configuration at the nucleation sites on substrates or within precursors. It is also suggested that the analogous titanium atomic arrangement between metallic titanium and rutile TiO_2 facilitates the vertical growth of rutile TiO_2 from the (001) plane of the TiO_2 film [32–34]. On the other hand, Ali et al. [35] described the hydrolysis of the TiO_2 precursor and the condensation process to advance through a balance of two key processes: olation and oxolation. The growth of highly crystalline TiO_2 nanorods is significantly influenced by process parameters such as precursor concentration, reaction duration, temperature, and subsequent annealing time [34,35].

Building upon the knowledge from earlier findings, the fabrication mechanism of GTNs is derived (Figure 3). During the hydrolysis process, titanium (IV) butoxide (TBOT) precursor reacts with water (H_2O). The coordination number of Ti^{4+} increases from +4 to +6 using its vacant d-orbitals to accept oxygen lone pairs forming Ti–O bonds [33,36]. Hydrolysis of the titanium precursor occurs, resulting in the exchange of butyl groups with hydroxyl (OH) groups [37]. The liberated protons (H^+) from the acid solution further react with the hydrolysed precursor, leading to the formation of the titanium hydroxide intermediate, TiOH^{2+} [19]. The protonated titanium hydroxide intermediates can readily condense through the interaction with hydroxyl groups (OH^-) on neighbouring TiO_6 octahedra. Subsequent dehydration (olation) steps, driven by the removal of water molecules (H_2O), lead to the formation of the TiO_2 nuclei. Notably, chloride ions (Cl^-) from the acidic solution play a crucial role in deprotonation (oxolation) processes, influencing the growth of the GTNs [38].

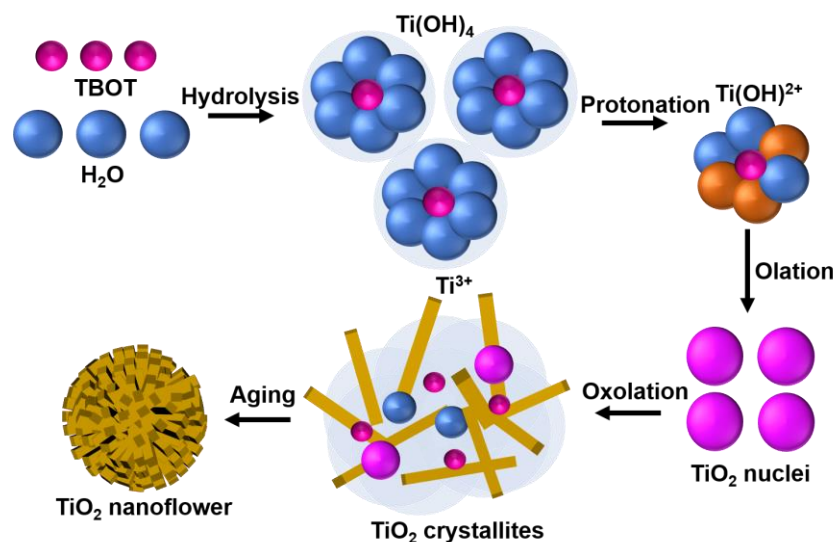
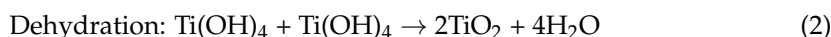
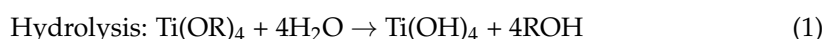
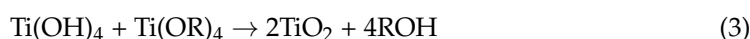


Figure 3. Schematic illustrations on the growth mechanism of GTNs.

The entire reaction sequences for the formation of GTNs via the hydrothermal process are as follows:



GTNs exhibit well-defined rutile TiO_2 nanostructures having a high surface area and abundant active sites, which promotes efficient oxidation and reduction reactions during photocatalytic dye degradation and gas sensing applications.

2.2. Photocatalytic Degradation of MB Dye

Figure 4a presents the investigation of the photocatalytic activity of rutile GTNs using the photodegradation of MB dye under UV light irradiation. Absorbance spectra shown in Figure 4a reveal that the GTNs exhibit excellent degradation performance with a 91% degradation of 5 ppm of MB dye within 160 min. The inset of Figure 4a displays the images of colour change during MB dye degradation. The photocatalytic degradation efficiency of GTNs was investigated at varying initial MB concentrations (1 ppm, 2.5 ppm, 5 ppm, 10 ppm, and 15 ppm) as shown in Figure 4b. The plot shows the normalized concentration (C/C_0) of MB versus irradiation time for GTNs with varying initial dye concentrations. Notably, 5 ppm of MB resulted in the highest degradation efficiency compared to other initial MB concentrations. Furthermore, the degradation rate follows a pseudo-first-order kinetic model, where the rate constant can be determined by [39] the following:

$$\ln(C/C_0) = -Kt \quad (5)$$

where C is the degraded concentration, C_0 is the initial concentration, K is the rate constant of the reaction, and time (t) is the degradation time.

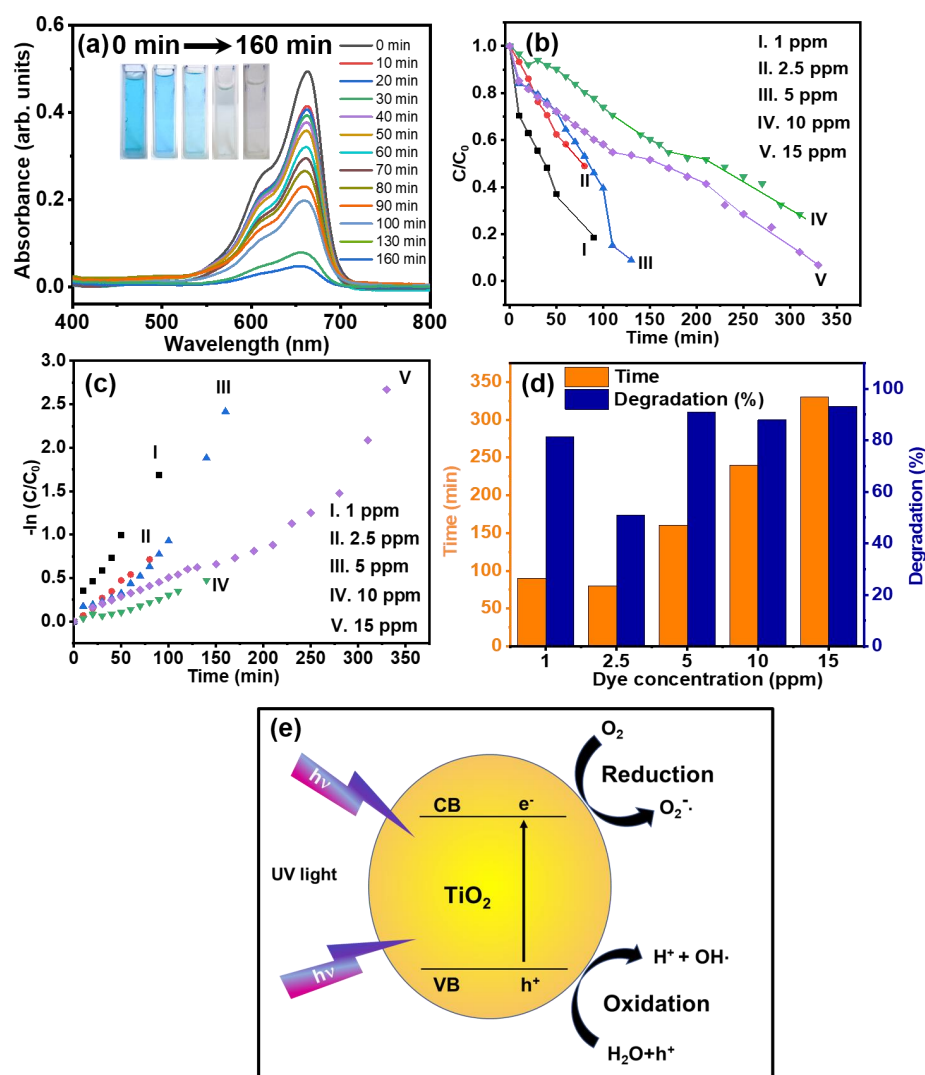


Figure 4. (a) UV-vis absorbance spectrum of MB (5 ppm), (b) photocatalytic degradation of MB (1 ppm, 2.5 ppm, 5 ppm, 10 ppm, and 15 ppm) under UV irradiation, (c) the rate constants for MB dye degradation, (d) the photocatalytic degradation (%) of MB dye at various concentrations, and (e) the photocatalytic dye degradation mechanism of GTNs.

The rate constants (k) for MB degradation were determined at various concentrations of dye as shown in Figure 4c. The rate constants followed a decreasing trend: $k(\text{MB}) = 0.017 \text{ min}^{-1}$ (1 ppm) > 0.009 min^{-1} (2.5 ppm) > 0.006 min^{-1} (5 ppm) > 0.004 min^{-1} (10 ppm) > 0.002 min^{-1} (15 ppm). The efficiency of MB dye degradation is determined by the following equation:

$$R = (C_0 - C)/C_0 \times 100\% \quad (6)$$

Figure 4d shows the degradation percentages of MB dye at various concentrations. The degradation achieved was 81% for 1 ppm in 90 min, 51% for 2.5 ppm in 80 min, 91% for 5 ppm in 160 min, 87% for 10 ppm in 240 min, and 71% for 15 ppm in 250 min, respectively. The highest degradation efficiency (91%) was achieved for 5 ppm MB within a relatively short irradiation time (160 min). The combined data from Figure 4c,d demonstrate that the photocatalytic degradation efficiency of MB is directly influenced by the concentration. Lower MB concentrations facilitate faster and more efficient degradation, while higher concentrations require longer irradiation times and achieve lower degradation efficiencies. This is because upon absorbing a photon with enough energy, an electron in the valence band of TiO_2 is excited to the conduction band. To elucidate the reasons behind the differences in photocatalytic activities, we must delve into the fundamental mechanism of semiconductor photocatalysis. Identifying the most effective nanomaterials for dye degradation requires a thorough evaluation of various parameters and the specific properties of the target dyes. Factors like composition, morphology, surface area, and crystallinity of nanomaterials play a crucial role in determining their degradation rate. Table 1. is provided to facilitate a clearer understanding of the photocatalytic MB dye degradation efficiency analysis across various nanomaterials (Such as $\text{MoO}_3/\text{TiO}_2/5\%\text{rGO}$, $\text{Fe}_2\text{O}_3/\text{TiO}_2$, Cu-CdS, Ag doped ZnO, ZnO-CNT, SnO_2 nanotubes, and different TiO_2 nanostructures) reveals distinct performance variations [40–48].

Table 1. Comparison table on the photocatalytic dye degradation efficiency of GTN catalyst with other reported catalysts.

Catalysts	Light Source/Dye	Degradation Time	Dye Degradation (%)	References
$\text{MoO}_3/\text{TiO}_2/5\%\text{rGO}$	UV light/MB	60 min	95%	[40]
$\text{Fe}_2\text{O}_3/\text{TiO}_2$	UV light/MB	60 min	95%	[41]
Cu-CdS	Xe light/MB	260 min	89%	[42]
Ag doped ZnO	500 W halogen lamp/MB	200 min	95%	[43]
ZnO-CNT	UV light/MB	120 min	93%	[44]
SnO_2 nanotubes	UV light/MB	180 min	80.2%	[45]
TiO_2 nanorods	UV light/MB	330 min	96%	[46]
TiO_2 decorated CNT	UV light/MB	180 min	85%	[47]
TiO_2	UV light/MB	180 min	40%	[47]
Degussa p25	Solar light/MB	120 min	57%	[48]
Globosa like TiO_2 nanostructures (GTNs)	UV light/MB	160 min	91%	Present work

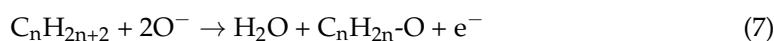
Packialakshmi et al. [49] demonstrated that the metal oxide nanocomposites ($\text{ZnO}/\text{SnO}_2/\text{rGO}$) displayed an enhanced photocatalytic dye degradation due to the synergistic interactions between the nanocomposites, resulting in improved charge separation and reduced recombination. Figure 4e shows a schematic representation of the photocatalytic mechanism of GTNs; the photocatalytic activity of GTNs indeed arises from the absorption of ultraviolet (UV) light below 387 nm, which corresponds to a band gap of 3.06 eV (cf. Figure 2d) [50,51]. Light absorption triggers the excitation of an electron (e^-) from the valence band (VB) to the conduction band (CB), creating a corresponding hole (h^+) in the VB. The photogenerated holes (h^+) possess strong oxidizing power and can react with surface-adsorbed water molecules (H_2O) and other pollutant species. This creates an electron-hole pair that can participate in redox reactions on the surface of the GTNs, leading to various photocatalytic activities [52]. The photocatalytic process initiates the generation of hydroxyl radicals ($\bullet\text{OH}$) and other highly oxidizing species (HOS), which effectively decompose and degrade organic pollutants into inert compounds, predominantly carbon dioxide (CO_2) and water (H_2O) [53]. The rate of electron-hole pair recombination depends on the light intensity and bandgap of the photocatalyst. The enhanced photocatalytic activity of GTNs can be attributed to their large surface

area and the abundance of active sites. These features facilitate a greater extent of reactant molecule adsorption, leading to a higher number of reaction sites and promoting efficient photocatalysis.

2.3. LPG Sensing

The rising popularity of LPG for cooking and industrial applications necessitates the development of reliable leak detection systems. LPG leakage causes accidents and affects the health of living beings due to it containing propane, butane, propylene, isobutane, and butylene. The accurate measurement of LPG leakage requires rapid and selective detection [54,55]. Aishwarya et al. [56] reported that the development of LPG sensors is paramount for public safety. The performance of LPG sensors can be improved using the synthesis method, fabrication technology, and dopant, catalyst, or advanced materials. The gas sensing mechanism relies on the adsorption and desorption of target gases on the surface of the sensing material. The GTNs hold significant potential as gas sensor materials owing to their high surface area, well-aligned architecture, and reduced agglomeration [57]. The LPG sensing performance of GTNs was systematically investigated by exposing them to LPG within a gas sensor unit. Figure 5a presents a schematic diagram of the gas sensing instrument, with GTNs employed as the sensing material and LPG used as the target gas. The target gas was diffused into the evacuated chamber at various concentrations (100 ppm, 500 ppm, and 1000 ppm). Experiments were conducted at different operational temperatures, including 40 °C, 100 °C, 200 °C, and 250 °C. As the operating temperature rises, increased thermal energy facilitates overcoming the activation energy barrier, leading to a linear augmentation in LPG response [54]. Figure 5b shows the sensing response (%) of the rutile GTNs at different ppm levels of LPG under various operating temperatures. At an operational temperature of 250 °C, the rutile GTNs exhibit a sensing response of 7.3%, 4.7%, and 3.1% to LPG concentrations of 100 ppm, 500 ppm, and 1000 ppm, respectively. The sensor demonstrates a pronounced enhancement in sensitivity as the concentration decreases. The diverse morphologies and distinct structure of the sensor offer ample and efficient gas diffusion channels along with active sites for gas molecule reactions [8]. The GTNs possess distinctive properties that enhance the adsorption and diffusion of target gas molecules both on its surface and within the interior regions of the TiO₂ nanostructures [57]. Upon exposure to the target gas, the sensor consistently achieved excellent response and recovery values, demonstrating exceptional reproducibility. Figure 5c,d show that at an operational temperature of 250 °C, the response times of GTNs are 10 s, 11 s, and 12 s for concentrations of 100 ppm, 500 ppm, and 1000 ppm, respectively. Correspondingly, the recovery times are 80 s, 134 s, and 142 s for the same concentrations. The enhanced repeatability and long-term stability in detecting trace amounts of LPG are ensured by the high surface area and well-defined architecture of TiO₂ nanostructures.

Tian et al. [8] reported that the gas sensing performance of TiO₂ is strongly influenced by its controllable morphology. TiO₂ nanostructures offer unique advantages such as increased surface area, faster electron transport, better gas permeability, and more active reaction sites. These factors collectively enhance TiO₂ gas sensor capabilities. The LPG sensing mechanism of TiO₂ is based on an oxidation and reduction reaction that occurs when the target gas interacts with the sensing material, and desorption of the gas molecules from the sensing material occurs when the temperature decreases [56,58]. When O₂ molecules adsorb onto the surface of the TiO₂ nanostructures, they extract electrons from the conduction band and subsequently trap them at the surface in the form of ions. The sensing mechanism of GTN sensors in air and under LPG exposure relies on the nature of the adsorbed oxygen ions, including O²⁻ (ads), O⁻ (ads), and O²⁻ (ads) on the film surfaces. These ionic species extract the electron from the conduction band [59]. The negative charge trapped in these oxygen species induces upward band bending, resulting in a substantial decrease in electrical resistance, consequently reducing the barrier height. The interaction between chemisorbed oxygen species and injected LPG molecules can be expressed as follows [2,54]:



where C_nH_{2n+2} represents CH_4 , C_3H_8 , and C_4H_{10} .

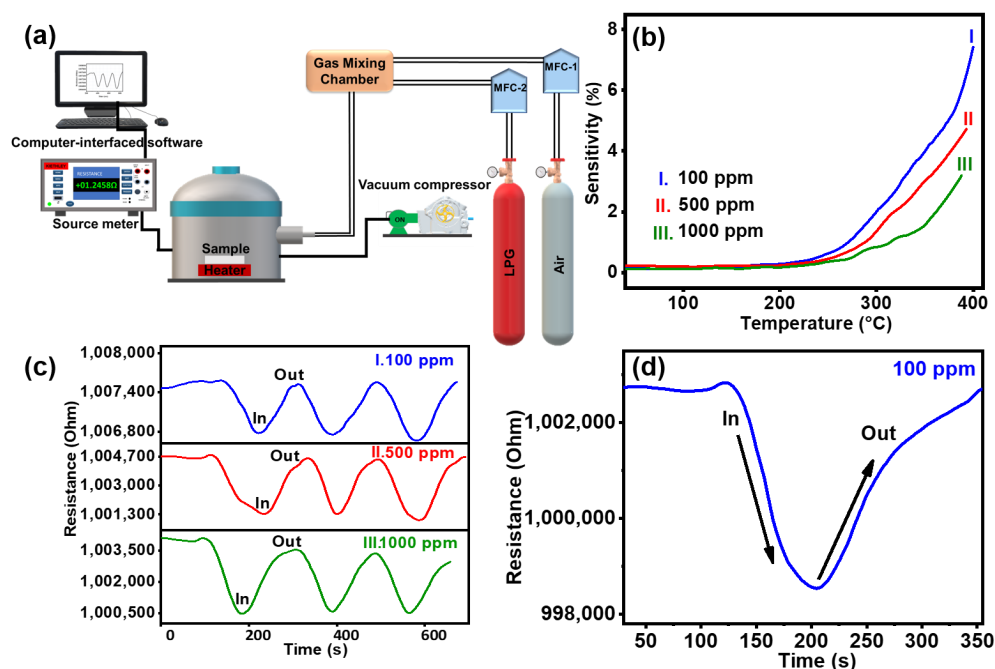


Figure 5. (a) Schematic of the LPG sensing instrument. (b) Sensitivity (%) of GTNs to LPG at different ppm levels. (c,d) Response time and recovery time of GTNs at 250 °C for concentrations of 100 ppm, 500 ppm, and 1000 ppm, respectively.

The reaction of these oxygen species with reducing gases, or the competitive adsorption and replacement of the adsorbed oxygen by other molecules, can decrease or even reverse the band bending. This results in a temporal change in the resistance of the TiO_2 nanostructured sensor. GTNs exhibit exceptional sensing characteristics for various concentrations of LPG, including good reproducibility, fast response times, and quick recovery times. These advantageous properties are attributed to the high surface area and well-defined architecture of the TiO_2 nanostructures, which offer numerous active sites for gas adsorption and interaction.

3. Materials and Methods

3.1. Materials

Hydrochloric acid (HCl) (Qualigens, Mumbai, India) (35.8–38.0 wt%), TBOT (Sigma-Aldrich, St. Louis, MO, USA), glass substrates, and distilled water were utilized in the preparation of TiO_2 nanostructures.

3.2. Hydrothermal Synthesis of GTNs

For the fabrication of GTNs, glass substrates with dimensions of 2×2 cm were employed. The substrates underwent a cleaning process involving ultrasonication in distilled water, acetone, and ethanol, each for a duration of 30 min. Prior to initiating the experiment, the hydrothermal autoclave reactor was thoroughly cleaned to prevent contamination. A total of 20 mL of HCl and 20 mL of deionized (DI) water, in a 1:1 ratio, was prepared. This solution was magnetically stirred at 500 rpm for 15 min at room temperature. Subsequently, 0.5 mL of TBOT was added dropwise over a period of 40 min, maintaining the room temperature throughout the process. The mixed solution was transferred into a Teflon liner (100 mL volume), and it was loaded in a hydrothermal autoclave reactor wherein the ultrasonically cleaned glass substrates were immersed. The deposition of GTNs was achieved by subjecting the autoclave to thermal treatment in a hot air oven at 150 °C for 12 h. This was followed by an aging process at ambient temperature for 24 h.

The samples were rinsed with DI water and then films were dried on a hot plate at 60 °C for 15 min.

3.3. Characterization

The crystal structure of the GTNs was determined using X-ray diffraction (XRD; Rigaku Instrument, Model-Ultima IV, Tokyo, Japan, X-ray diffractometer) using Cu K α radiation ($\lambda = 1.54056 \text{ \AA}$). The surface morphologies and elemental composition analysis of the samples were observed using field-emission scanning electron microscopy (FESEM; JSM-IT 800, JEOL, Tokyo, Japan) with an accelerated potential of 15 kV; energy-dispersive X-ray analysis (EDAX; ELECT SUPER, JSM IT300, Pleasanton, CA, USA); high-resolution transmission electron microscopy (HRTEM; JEM-F200 200 kV, JEOL, Tokyo, Japan); a Raman spectrometer (Renishaw Plc, Wotton-under-Edge, UK, inVia with a 532 nm laser); and a Fourier-transformed infrared spectrometer (FTIR, BRUKER ALPHA II, Billerica, MA, USA, ATR Mode) recorded in the 4000 cm^{-1} to 400 cm^{-1} was used to identify the functional groups. UV-visible transmittance of GTNs was recorded on a UV-vis-near-infrared spectrophotometer (UV-VIS-NIR; Agilent instrument, Cary 5000, Santa Clara, CA, USA) to estimate the band gap of GTNs.

3.4. Photocatalytic Dye Degradation of MB Dye

Photocatalytic activity of GTNs was examined by using MB (MB; $\text{C}_{16}\text{H}_{18}\text{ClN}_3\text{S}\cdot\text{xH}_2\text{O}$) dye. A series of MB stock solutions with varying initial concentrations (1 mg/L, 2.5 mg/L, 5 mg/L, 10 mg/L, and 15 mg/L) were prepared via serial dilutions in double-distilled water for the photocatalytic dye degradation experiments. The degradation of MB was performed using various initial concentrations; aliquots of 4 mL each were prepared from MB solutions with concentrations of 1 ppm, 2.5 ppm, 5 ppm, 10 ppm, and 15 ppm. These were then introduced into a 100 mL quartz beaker containing a 10 mm \times 10 mm catalyst within a fabricated reactor. A custom photocatalytic reactor was designed for the experiments, which consists of UV-C (Philips TUV 8 W G8T5) sources positioned at the top to irradiate the test solution placed in a beaker at the bottom. The distance between the UV light source and the test solution surface was maintained at a constant 10 cm. The photocatalyst and an aqueous dye solution were kept in the dark for 30 min to achieve equilibrium adsorption of the dye molecules onto the catalyst surface. The photocatalytic activity of hydrothermally prepared GTNs was evaluated under UV light irradiation. The concentration of MB was recorded at 663 nm using a UV-visible spectrometer (UV-1700, Shimadzu, Kyoto, Japan). Absorbance spectra were recorded at 10 min intervals to monitor dye degradation. These spectral measurements were utilized to evaluate the progression and degree of degradation.

3.5. LPG Sensing

LPG sensing experiments were carried out in a custom-made gas sensing chamber. The GTNs sample was positioned within a sealed chamber, and electrical contacts were created on the film surface using silver paste. The operating temperature varied from room temperature to 400 °C, monitored by a thermocouple. The samples were subjected to heating during the measurements. A pre-mixed gas stream containing LPG diluted in air at varying concentrations (ppm) was injected into the chamber using mass flow controllers. A source meter (Keithley 6430; Solon, OH, USA), interfaced with computer software, was employed to control the instrument. The LPG sensing characteristics and sensing responses were recorded by monitoring the changes in resistance with temperature variations at different LPG concentrations of 100 ppm, 500 ppm, and 1000 ppm. Sensitivity (%) was calculated using Equation (8), where resistance of air (R_{air}) and resistance of gas (R_{gas}) under various conditions was calculated.

$$\text{Sensitivity Response (\%)} = (R_{\text{air}} - R_{\text{gas}})/R_{\text{gas}} \times 100 \quad (8)$$

After the gas sensing experiment, the sample was heated at 400 °C for 30 min to desorb the species on the film surface, enhancing reproducibility.

4. Conclusions

Globosa-like TiO₂ nanostructures were synthesized using a simple and cost-effective hydrothermal method. Structural and compositional analyses confirmed the formation of single-crystalline rutile TiO₂ with characteristic Ti-O and Ti-O-Ti bonds with a direct optical bandgap of 3.06 eV. The growth mechanism on the formation of globosa-like TiO₂ nanostructures was derived. The photocatalytic degradation performance of the TiO₂ nanostructures was evaluated across a range of MB concentrations from 1 to 15 ppm. The nanostructures exhibited a significant MB dye degradation efficiency of approximately 91% within 160 minutes under UV light irradiation. Lower MB concentrations facilitated enhanced and accelerated degradation, whereas higher concentrations resulted in prolonged irradiation times and reduced degradation efficiency. Additionally, the nanostructures showed a 7.3% sensing response to 100 ppm LPG at 250°C, with rapid response and recovery times. The enhanced surface area and well-defined architecture synergistically contributed to attain remarkable photocatalytic and LPG sensing performance.

Supplementary Materials: The following supporting information can be downloaded at: <https://www.mdpi.com/article/10.3390/molecules29174063/s1>, Figure S1: (a) Plain-view FESEM image of GTNs. (b) Schematic representation of the FESEM plot profile, (c–e) different surface area plot analysis (ImageJ Software-1.54j version) of GTNs [60–62].

Author Contributions: M.S.R.: conceptualization, investigation, validation, writing—original draft, visualization, and data curation. B.R.: conceptualization, methodology, investigation, writing—review and editing, visualization, supervision, and funding acquisition. G.P.O.: conceptualization, writing—review and editing, and visualization. R.S.: conceptualization, writing—review and editing, and visualization. B.P.: conceptualization, methodology, investigation, writing—original draft, writing—review and editing, visualization, and supervision. K.J.S.: conceptualization, methodology, investigation, writing—original draft, writing—review and editing, visualization, supervision, funding acquisition, and supervision. All authors have read and agreed to the published version of the manuscript.

Funding: This research received no external funding.

Institutional Review Board Statement: Not applicable.

Informed Consent Statement: Not applicable.

Data Availability Statement: Data will be made available upon request.

Acknowledgments: Mutchu Shanmukha Rao is grateful for the financial support provided by the University Grants Commission, India (UGC-JRF/SRF), Senior research Fellowship award. The authors would like to thank the financial support of the Science and Engineering Research Board (SERB), India, and the CSIR-Institute of Minerals and Materials Technology, India, via Research Project GAP-336, OLP-106, and SSP-453.

Conflicts of Interest: The authors declare no conflicts of interest.

References

1. Vaiano, V. *Visible-Light-Active Photocatalysts for Environmental Remediation and Organic Synthesis*; MDPI: Basel, Switzerland, 2021; Volume 1, ISBN 9783036536484.
2. Wetchakun, K.; Samerjai, T.; Tamaekong, N.; Liewhiran, C.; Siri Wong, C.; Kruefu, V.; Wisitsoraat, A.; Tuantranont, A.; Phanichphant, S. Semiconducting Metal Oxides as Sensors for Environmentally Hazardous Gases. *Sens. Actuators B Chem.* **2011**, *160*, 580–591. [[CrossRef](#)]
3. Varghese, O.K.; Grimes, C.A. Metal Oxide Nanoarchitectures for Environmental Sensing. *J. Nanosci. Nanotechnol.* **2003**, *3*, 277–293. [[CrossRef](#)]
4. Sun, X.; Wang, C.; Su, D.; Wang, G.; Zhong, Y. Application of Photocatalytic Materials in Sensors. *Adv. Mater. Technol.* **2020**, *5*, 1900993. [[CrossRef](#)]
5. Jada, N.; Sankaran, K.J.; Sakthivel, R.; Sethi, D.; Mohapatra, P. Synergistic Effect of MoO₃/TiO₂ towards Discrete and Simultaneous Photocatalytic Degradation of *E. Coli* and Methylene Blue in Water. *Bull. Mater. Sci.* **2021**, *44*, 167. [[CrossRef](#)]
6. Verma, R.; Gangwar, J.; Srivastava, A.K. Multiphase TiO₂ Nanostructures: A Review of Efficient Synthesis, Growth Mechanism, Probing Capabilities, and Applications in Bio-Safety and Health. *RSC Adv.* **2017**, *7*, 44199–44224. [[CrossRef](#)]

7. Chen, X.; Mao, S.S. Titanium Dioxide Nanomaterials: Synthesis, Properties, Modifications and Applications. *Chem. Rev.* **2007**, *107*, 2891–2959. [[CrossRef](#)]
8. Tian, X.; Cui, X.; Lai, T.; Ren, J.; Yang, Z.; Xiao, M.; Wang, B.; Xiao, X.; Wang, Y. Nano Materials Science Gas Sensors Based on TiO₂ Nanostructured Materials for the Detection of Hazardous Gases: A Review. *Nano Mater. Sci.* **2021**, *3*, 390–403. [[CrossRef](#)]
9. Almohamadi, H.; Awad, S.A.; Sharma, A.K.; Fayzullaev, N. Photocatalytic Activity of Metal- and Non-Metal-Anchored ZnO and TiO₂ Nanocatalysts for Advanced Photocatalysis: Comparative Study. *Catalysts* **2024**, *14*, 420. [[CrossRef](#)]
10. Mahanta, S.K.; Suman, S.; Ghadei, S.K.; Balaji, U.; Sakthivel, R.; Sankaran, K.J. Direct Fabrication of Metal-Free Graphene Nanohairs/Polyimide Heterojunction for the Highly Efficient Photocatalytic Degradation of Industrial Dyes. *Diam. Relat. Mater.* **2023**, *137*, 110096. [[CrossRef](#)]
11. Nakata, K.; Fujishima, A. TiO₂ Photocatalysis: Design and Applications. *J. Photochem. Photobiol. C Photochem. Rev.* **2012**, *13*, 169–189. [[CrossRef](#)]
12. Hao, B.; Guo, J.; Zhang, L.; Ma, H. Magnetron Sputtered TiO₂/CuO Heterojunction Thin Films for Efficient Photocatalysis of Rhodamine B. *J. Alloys Compd.* **2022**, *903*, 163851. [[CrossRef](#)]
13. Crespo-Monteiro, N.; Hamandi, M.; Higueta, M.A.U.; Guillard, C.; Dappozze, F.; Jamon, D.; Vocanson, F.; Jourlin, Y. Influence of the Micro-Nanostructuring of Titanium Dioxide Films on the Photocatalytic Degradation of Formic Acid under UV Illumination. *Nanomaterials* **2022**, *12*, 1008. [[CrossRef](#)]
14. Zhao, J.; Wang, H.; Cai, Y.; Zhao, J.; Gao, Z.; Song, Y.Y. The Challenges and Opportunities for TiO₂ Nanostructures in Gas Sensing. *ACS Sens.* **2024**, *9*, 1644–1655. [[CrossRef](#)] [[PubMed](#)]
15. Zakrzewska, K.; Radecka, M. TiO₂-Based Nanomaterials for Gas Sensing—Influence of Anatase and Rutile Contributions. *Nanoscale Res. Lett.* **2017**, *12*, 89. [[CrossRef](#)]
16. Lee, P.Y.; Widyastuti, E.; Lin, T.C.; Chiu, C.T.; Xu, F.Y.; Tseng, Y.T.; Lee, Y.C. The Phase Evolution and Photocatalytic Properties of a Ti-TiO₂ Bilayer Thin Film Prepared Using Thermal Oxidation. *Coatings* **2021**, *11*, 808. [[CrossRef](#)]
17. Zharvan, V.; Daniyati, R.; Nur Ichzan, A.S.; Yudoyono, G. Darminto Study on Fabrication of TiO₂ Thin Films by Spin-Coating and Their Optical Properties. *AIP Conf. Proc.* **2016**, *1719*, 030018. [[CrossRef](#)]
18. Nakate, U.T.; Yu, Y.T.; Park, S. Hydrothermal Synthesis of ZnO Nanoflakes Composed of Fine Nanoparticles for H₂S Gas Sensing Application. *Ceram. Int.* **2022**, *48*, 28822–28829. [[CrossRef](#)]
19. Gupta, T.; Samriti; Cho, J.; Prakash, J. Hydrothermal Synthesis of TiO₂ Nanorods: Formation Chemistry, Growth Mechanism, and Tailoring of Surface Properties for Photocatalytic Activities. *Mater. Today Chem.* **2021**, *20*, 100428. [[CrossRef](#)]
20. Abd-Elnaiem, A.M.; Hakamy, A.; Afify, N.; Omer, M.; Abdelbaki, R.F. Nanoarchitectonics of Zinc Nickel Ferrites by the Hydrothermal Method for Improved Structural and Magnetic Properties. *J. Alloys Compd.* **2024**, *984*, 173941. [[CrossRef](#)]
21. Hameed, N.A.; Ali, I.M.; Hassun, H.K. Calculating Surface Roughness for a Large Scale Sem Images by Mean of Image Processing. *Energy Procedia* **2019**, *157*, 84–89. [[CrossRef](#)]
22. Makarem, R.; Cristiano, F.; Muller, D.; Fazzini, P.F. An Improved STEM/EDX Quantitative Method for Dopant Profiling at the Nanoscale. *Microsc. Microanal.* **2020**, *26*, 76–85. [[CrossRef](#)] [[PubMed](#)]
23. Dennis, P.F. Oxygen Self-Diffusion in Quartz Under Hydrothermal Conditions. *J. Geophys. Res.* **1984**, *89*, 4047–4057. [[CrossRef](#)]
24. Samriti; Prateek; Joshi, M.C.; Gupta, R.K.; Prakash, J. Hydrothermal Synthesis and Ta Doping of TiO₂ Nanorods: Effect of Soaking Time and Doping on Optical and Charge Transfer Properties for Enhanced SERS Activity. *Mater. Chem. Phys.* **2022**, *278*, 125642. [[CrossRef](#)]
25. Swamy, V.; Muddle, B.C.; Dai, Q. Size-Dependent Modifications of the Raman Spectrum of Rutile TiO₂. *Appl. Phys. Lett.* **2006**, *89*, 163118. [[CrossRef](#)]
26. Chowdhury, S.; King, N.; Wong-Ng, W. Rutile TiO₂ bulk Structural and Vibrational Properties: A DFT Study on the Importance of Pseudopotentials. *arXiv* **2018**, arXiv:1811.03783.
27. Wilson, G.J.; Matijasevich, A.S.; Mitchell, D.R.G.; Schulz, J.C.; Will, G.D. Modification of TiO₂ for Enhanced Surface Properties: Finite Ostwald Ripening by a Microwave Hydrothermal Process. *Langmuir* **2006**, *22*, 2016–2027. [[CrossRef](#)] [[PubMed](#)]
28. Gomathi Thanga Keerthana, B.; Solaiyammal, T.; Muniyappan, S.; Murugakoothan, P. Hydrothermal Synthesis and Characterization of TiO₂ Nanostructures Prepared Using Different Solvents. *Mater. Lett.* **2018**, *220*, 20–23. [[CrossRef](#)]
29. Miao, L.; Jin, P.; Kaneko, K.; Terai, A.; Nabatova-Gabain, N.; Tanemura, S. Preparation and Characterization of Polycrystalline Anatase and Rutile TiO₂ Thin Films by Rf Magnetron Sputtering. *Appl. Surf. Sci.* **2003**, *212–213*, 255–263. [[CrossRef](#)]
30. Tang, J.F.; Su, H.H.; Lu, Y.M.; Chu, S.Y. Controlled Growth of ZnO Nanoflowers on Nanowall and Nanorod Networks via a Hydrothermal Method. *CrystEngComm* **2015**, *17*, 592–597. [[CrossRef](#)]
31. Peng, H.; Liu, Y.; Shen, Y.; Xu, L.; Lu, J.; Li, M.; Lu, H.L.; Gao, L. Highly Sensitive and Selective Toluene Gas Sensors Based on ZnO Nanoflowers Decorated with Bimetallic AuPt. *Molecules* **2024**, *29*, 1657. [[CrossRef](#)]
32. Yang, X.; Jin, C.; Liang, C.; Chen, D.; Wu, M.; Yu, J.C. Nanoflower Arrays of Rutile TiO₂. *Chem. Commun.* **2011**, *47*, 1184–1186. [[CrossRef](#)] [[PubMed](#)]
33. Ye, M.; Liu, H.Y.; Lin, C.; Lin, Z. Hierarchical Rutile TiO₂ Flower Cluster-Based High Efficiency Dye-Sensitized Solar Cells via Direct Hydrothermal Growth on Conducting Substrates. *Small* **2013**, *9*, 312–321. [[CrossRef](#)]
34. Liu, B.; Enache-Pommer, E.; Aydil, E.S. Oriented Single-Crystalline Rutile TiO₂ Nanorods on Transparent Conducting Substrates for Dye-Sensitized Solar Cells. In Proceedings of the 10AICHE—2010 AICHE Annual Meeting Conference Proceedings, Salt Lake City, UT, USA, 7–12 November 2010; Volume 1.

35. Ali, W.; Jaffari, G.H.; Khan, S.; Liu, Y. Morphological Control of 1D and 3D TiO₂ Nanostructures with Ammonium Hydroxide and TiO₂ Compact Layer on FTO Coated Glass in Hydrothermal Synthesis. *Mater. Chem. Phys.* **2018**, *214*, 48–55. [[CrossRef](#)]
36. Prathan, A.; Sanglao, J.; Wang, T.; Bhoomanee, C.; Ruankham, P.; Gardchareon, A.; Wongratanaphisan, D. Controlled Structure and Growth Mechanism behind Hydrothermal Growth of TiO₂ Nanorods. *Sci. Rep.* **2020**, *10*, 8065. [[CrossRef](#)]
37. López Zavala, M.Á.; Lozano Morales, S.A.; Ávila-Santos, M. Synthesis of Stable TiO₂ Nanotubes: Effect of Hydrothermal Treatment, Acid Washing and Annealing Temperature. *Heliyon* **2017**, *3*, e00456. [[CrossRef](#)] [[PubMed](#)]
38. Jordan, V.; Javornik, U.; Plavec, J.; Podgornik, A.; Rečnik, A. Self-Assembly of Multilevel Branched Rutile-Type TiO₂ Structures via Oriented Lateral and Twin Attachment. *Sci. Rep.* **2016**, *6*, 24216. [[CrossRef](#)]
39. Matouq, M.; Al-Anber, Z.; Susumu, N.; Tagawa, T.; Karapanagioti, H. The Kinetic of Dyes Degradation Resulted from Food Industry in Wastewater Using High Frequency of Ultrasound. *Sep. Purif. Technol.* **2014**, *135*, 42–47. [[CrossRef](#)]
40. Al-Otaibi, A.L.; Elsayed, K.A.; Manda, A.A.; Haladu, S.A.; Ibrahim Gaya, U.; Ercan, F.; Kayed, T.S.; Çevik, E.; Alhajri, U.; Ercan, İ.; et al. Pulsed Laser Ablation-Mediated Facile Fabrication of MoO₃/TiO₂/RGO Nanocomposite as a Photocatalyst for Dye Degradation. *Opt. Laser Technol.* **2024**, *170*, 110156. [[CrossRef](#)]
41. Ahmed, M.A.; El-Katori, E.E.; Gharni, Z.H. Photocatalytic Degradation of Methylene Blue Dye Using Fe₂O₃/TiO₂ Nanoparticles Prepared by Sol-Gel Method. *J. Alloys Compd.* **2013**, *553*, 19–29. [[CrossRef](#)]
42. Al-Jawad, S.M.H.; Aboud, K.H.; Imran, N.J.; Taher, S.Y. Copper Doping of CdS Nanoflakes and Nanoflowers for Efficient Photocatalytic Degradation of MB and MV Dyes. *Plasmonics* **2024**, 15571963. [[CrossRef](#)]
43. Shelar, S.G.; Mahajan, V.K.; Patil, S.P.; Sonawane, G.H. Effect of Doping Parameters on Photocatalytic Degradation of Methylene Blue Using Ag Doped ZnO Nanocatalyst. *SN Appl. Sci.* **2020**, *2*, 820. [[CrossRef](#)]
44. Chaudhary, D.; Singh, S.; Vankar, V.D.; Khare, N. ZnO Nanoparticles Decorated Multi-Walled Carbon Nanotubes for Enhanced Photocatalytic and Photoelectrochemical Water Splitting. *J. Photochem. Photobiol. A Chem.* **2018**, *351*, 154–161. [[CrossRef](#)]
45. Sadeghzadeh-Attar, A. Efficient Photocatalytic Degradation of Methylene Blue Dye by SnO₂ Nanotubes Synthesized at Different Calcination Temperatures. *Sol. Energy Mater. Sol. Cells* **2018**, *183*, 16–24. [[CrossRef](#)]
46. Anwar, M.S.; Danish, R.; Koo, B.H. Hierarchical Flower-like Nanostructures of Rutile TiO₂ and Their Photocatalytic Activity. *J. Nanosci. Nanotechnol.* **2016**, *16*, 12851–12855. [[CrossRef](#)]
47. Akhter, P.; Ali, F.; Ali, A.; Hussain, M. TiO₂ Decorated CNTs Nanocomposite for Efficient Photocatalytic Degradation of Methylene Blue. *Diam. Relat. Mater.* **2024**, *141*, 110702. [[CrossRef](#)]
48. Xu, H.; Li, G.; Zhu, G.; Zhu, K.; Jin, S. Enhanced Photocatalytic Degradation of Rutile/Anatase TiO₂ Heterojunction Nanoflowers. *Catal. Commun.* **2015**, *62*, 52–56. [[CrossRef](#)]
49. Packialakshmi, J.S.; Albeshr, M.F.; Alrefaei, A.F.; Zhang, F.; Liu, X.; Selvankumar, T.; Mythili, R. Development of ZnO/SnO₂/RGO Hybrid Nanocomposites for Effective Photocatalytic Degradation of Toxic Dye Pollutants from Aquatic Ecosystems. *Environ. Res.* **2023**, *225*, 115602. [[CrossRef](#)]
50. Kim, M.G.; Kang, J.M.; Lee, J.E.; Kim, K.S.; Kim, K.H.; Cho, M.; Lee, S.G. Effects of Calcination Temperature on the Phase Composition, Photocatalytic Degradation, and Virucidal Activities of TiO₂ Nanoparticles. *ACS Omega* **2021**, *6*, 10668–10678. [[CrossRef](#)]
51. Wang, Y.; Zhang, L.; Deng, K.; Chen, X.; Zou, Z. Low Temperature Synthesis and Photocatalytic Activity of Rutile TiO₂ Nanorod Superstructures. *J. Phys. Chem. C* **2007**, *111*, 2709–2714. [[CrossRef](#)]
52. Wu, J.M.; Huang, B.; Wang, M.; Osaka, A. Titania Nanoflowers with High Photocatalytic Activity. *J. Am. Ceram. Soc.* **2006**, *89*, 2660–2663. [[CrossRef](#)]
53. Molina-Reyes, J.; Romero-Moran, A.; Uribe-Vargas, H.; Lopez-Ruiz, B.; Sanchez-Salas, J.L.; Ortega, E.; Ponce, A.; Morales-Sanchez, A.; Lopez-Huerta, F.; Zuñiga-Islas, C. Study on the Photocatalytic Activity of Titanium Dioxide Nanostructures: Nanoparticles, Nanotubes and Ultra-Thin Films. *Catal. Today* **2020**, *341*, 2–12. [[CrossRef](#)]
54. Dhawale, D.S.; Gujar, T.P.; Lokhande, C.D. TiO₂ Nanorods Decorated with Pd Nanoparticles for Enhanced Liquefied Petroleum Gas Sensing Performance. *Anal. Chem.* **2017**, *89*, 8531–8537. [[CrossRef](#)] [[PubMed](#)]
55. Sankaran, K.J.; Suman, S.; Sahaw, A.; Balaji, U.; Sakthivel, R. Improved LPG Sensing Properties of Nickel Doped Cobalt Ferrites Derived from Metallurgical Wastes. *J. Magn. Magn. Mater.* **2021**, *537*, 168231. [[CrossRef](#)]
56. Aishwarya, K.; Nirmala, R.; Navamathavan, R. Recent Advancements in Liquefied Petroleum Gas Sensors: A Topical Review. *Sens. Int.* **2021**, *2*, 100091. [[CrossRef](#)]
57. Lee, J.H. Gas Sensors Using Hierarchical and Hollow Oxide Nanostructures: Overview. *Sens. Actuators B Chem.* **2009**, *140*, 319–336. [[CrossRef](#)]
58. Ramanavicius, S.; Jagminas, A.; Ramanavicius, A. Gas Sensors Based on Titanium Oxides (Review). *Coatings* **2022**, *12*, 699. [[CrossRef](#)]
59. Patil, L.A.; Suryawanshi, D.N.; Pathan, I.G.; Patil, D.M. Nickel Doped Spray Pyrolyzed Nanostructured TiO₂ Thin Films for LPG Gas Sensing. *Sens. Actuators B Chem.* **2013**, *176*, 514–521. [[CrossRef](#)]
60. Smith, M.F.; Limwichean, S.; Horprathum, M.; Chairprapa, J.; Aye, W.W.; Chananonnawathorn, C.; Patthanasettakul, V.; Eiamchai, P.; Nuntawong, N.; Klamchuen, A. Determination of density and specific surface area of nanostructured zinc oxide films by X-ray fluorescence and scanning electron microscopy. *Thin Solid Films* **2022**, *751*, 139207.

61. Bhushan, B. Surface roughness analysis and measurement techniques. In *Modern Tribology Handbook, Two Volume Set*; CRC press: Boca Raton, FL, USA, 2000; pp. 49–119.
62. Sliz, R.; Eneh, C.; Suzuki, Y.; Czajkowski, J.; Fabritius, T.; Kathirgamanathan, P.; Nathan, A.; Myllyla, R.; Jabbour, G. Large area quantitative analysis of nanostructured thin-films. *RSC Adv.* **2015**, *5*, 12409–12415. [[CrossRef](#)]

Disclaimer/Publisher’s Note: The statements, opinions and data contained in all publications are solely those of the individual author(s) and contributor(s) and not of MDPI and/or the editor(s). MDPI and/or the editor(s) disclaim responsibility for any injury to people or property resulting from any ideas, methods, instructions or products referred to in the content.